Original Article
J. Korean Wood Sci. Technol. 2022, 50(4): 219-236
https://doi.org/10.5658/WOOD.2022.50.4.219

Journal of the Korean Wood Science and Technology
pISSN: 1017-0715 eISSN: 2233-7180
http://www.woodj.org

Nanocomposite Electrode Materials Prepared from *Pinus roxburghii* and Hematite for Application in Supercapacitors

Dibyashree SHRESTHA[1,†]

ABSTRACT

Wood-based nanocomposite electrode materials were synthesized for application in supercapacitors by mixing nanostructured hematite (Fe_2O_3) with highly porous activated carbon (AC) produced from the wood-waste of *Pinus roxburghii*. The AC was characterized using various instrumental techniques and the results showed admirable electrochemical properties, such as high surface area and reasonable porosity. Firstly, AC was tested as an electrode material for supercapacitors and it showed a specific capacitance of 59.02 Fg^{-1} at a current density of 1 Ag^{-1}, cycle life of 84.2% after 1,000 cycles (at a current density of 3 Ag^{-1}), and energy density of 5.1 Wh/kg at a power density of 135 Wkg^{-1}. However, when the AC was composited with different ratios of Fe_2O_3 (1:1, 2:1, and 1:2), there was an overall improvement in its electrochemical performance. Among the 3 ratios, 2:1 (AC:Fe_2O_3) had the best specific capacitance of 102.42 Fg^{-1} at 1 Ag^{-1}, cycle life of 94.4% capacitance after 1,000 cycles (at a current density of 3 Ag^{-1}), and energy density of 8.34 Wh/kg at a power density of 395.15 Wkg^{-1} in 6 M KOH electrolyte in a 3-electrode experimental setup with a high working voltage of 1.55 V. Furthermore, when Fe_2O_3 was doubled, 1:2 (AC:Fe_2O_3), the electrochemical capacitive performance of the electrode twisted and deteriorated due to either the accumulation of Fe_2O_3 particles within the composite or higher bulk resistance value of pure Fe_2O_3.

Keywords: *Pinus roxburghii,* hematite, nanocomposite, energy density, supercapacitor

1. INTRODUCTION

The popular *Pinus roxburghii*, which belongs to the family Pinaceae, is locally known as “Salla”. Pinaceae leaves are long and needle-shaped, and the trees are evergreen conifers (Almendros *et al*., 2015). They are grown for commercial and industrial uses, such as soft timber, carpentry furniture, window frames, paneling floors, walls, and roofs, and some species are used as an important source of turpentine, pulp, or tar. Furthermore, different parts of these trees, such as barks, leaves, and cones are utilized for firewood (Hwang *et al*., 2021a). Therefore, Pinewood waste is a promising source of raw materials for producing porous carbon, which can be a novel material for energy storing devices.

Morphologically, Pinewood is composed of well-oriented microfibers with fiber cells that have distinctly mesoporous structures with tracheids that are used to transport water, ion, and oxygen during metabolism. Based on the chemical composition, these trees are also

Date Received March 10, 2022, Date Revised April 26, 2022, Date Accepted May 30, 2022
[1] Department of Chemistry, Patan Multiple Campus, Tribhuvan University, Patan Dhoka, Lalitpur 44613, Nepal
[†] Corresponding author: Dibyashree Shrestha (e-mail: shresthadibyashree@gmail.com, https://orcid.org/0000-0002-9028-6668)

an abundant source of lignocellulosic carbonaceous materials (Mondal *et al*., 2017). They contain 3 major structural components, cellulose, hemicellulose, and lignin, that are widely distributed throughout vascular plants where they form the structural support system and play a vital role in creating porosity. The amount of each component depends on features like the species, age, and the part of the plant from which it is extracted (Fengel and Wegener, 1983; Schulz *et al*., 2021). However, *Pinus roxburghii*, being a softwood, contains 45%–50% cellulose, 25%–35% hemicellulose, and 25%–35% lignin (Fan *et al*., 1982). Additionally, these woods have also been utilized for the adsorption of impurities from water (Shen *et al*., 2021).

Herein, we report the use of wood waste from local carpentry shops to prepare activated carbon (AC) for use in energy storage devices, such as supercapacitors. ACs are incredible and essential energy storage materials because of their high conductivity, high surface area, high porosity, low cost, and availability (Iswanto *et al*., 2021; Shen *et al*., 2021). Supercapacitors are poised to replace batteries because of their superior properties, such as fast charge–discharge capability, long working lifetime, and safety record (Kim *et al*., 2019; Zhang *et al*., 2015). Therefore, modern portable electronic devices, electrical vehicles, military weapons, space equipment, and several electrical devices demand the use of supercapacitors (Chen *et al*., 2020; Liu *et al*., 2016). Many researchers have investigated the wide applications of supercapacitors prepared from different wood-based precursors using different activation processes (Mohamed *et al*., 2020; Wang *et al*., 2019; Zhang *et al*., 2019).

In supercapacitors, charge storage takes place at the surface of the electrodes either through adsorption of ions into the pores of the electrode materials (i.e., electric double layer capacity (EDLC) or nonfaradaic capacitive charge) or surface redox reactions at the interface (i.e., pseudocapacitive or faradaic capacitive charge; Aadil *et al*., 2020; Chen *et al*., 2020). EDLC-type electrode materials produce high power density and longer life cycle retention but have low energy density (Wei *et al*., 2020), while pseudocapacitive materials provide high energy density but have low cycle stability (Krishnamoorthy *et al*., 2020).

A recent trend in enhancing the capacity and life of supercapacitor materials is to combine both types of charge storage mechanisms (i.e., EDLC and pseudocapacitive), to yield a hybrid-supercapacitor (Liu *et al*., 2017; Wong *et al*., 2020).

ACs are used as negative electrodes (cathodes) in EDLC to accumulate energy (Galih *et al*., 2020; Wang *et al*., 2019). Recent studies report that higher charge storage capacities can be delivered by pseudocapacitive anodes, such as transitional metal oxides like MoO_3 (Zhang *et al*., 2019), V_2O_5 (Guo *et al*., 2015), WO_3 (Yun *et al*., 2019), TiN (Sun *et al*., 2020), Fe_3O_4 (Arun *et al*., 2019), FeOOH (Chen *et al*., 2016), and Fe_2O_3 (Zhang *et al*., 2020), than by carbon materials. Moreover, hematite (Fe_2O_3) is considered an efficient transition metal oxide for the preparation of supercapacitor electrode materials (Li *et al*., 2019) owing to its many advantages, such as cost-effectiveness, natural abundance, excellent physicochemical stability, minimal environmental impact, large theoretical capacitance (3,625 Fg^{-1}), and a high potential for hydrogen evolution in aqueous solution. Irrespectively, Fe_2O_3 electrode material has serious disadvantages, such as poor electrical conductivity and large volume change, reduction in the rate capacity and lifespan due to volume expansion, restricting its applications in high-power storage devices. However, incorporating AC with metal oxides, such as Fe_2O_3, is an alternative way of improving its conductivity. This leads to better ion diffusion and enhanced overall electrochemical properties compared with that of the individual components because of the synergistic effect between the metal oxide (Fe_2O_3) and AC (Xuan *et al*., 2020; Yang *et al*., 2020).

Hence, in this research, AC prepared from locally available *Pinus roxburghii* wood waste (carpentry waste)

was used as a precursor for preparing a hybrid-supercapacitor electrode material with Fe_2O_3. The AC prepared was characterized using different instrumental techniques, such as X-ray diffraction (XRD), Fourier transform infrared spectroscopy (FTIR), X-ray photoelectron spectroscopy (XPS), Raman spectroscopy, scanning electron microscopy (SEM), and Brunauer–Emmett–Teller (BET) theory to understand the effects on the surface morphology, functionality, and porosity that are essential for exhibiting admirable electrochemical behavior. Thereafter, the AC was electrochemically characterized using cyclic voltammetry (CV), galvanostatic charge/discharge (GCD), and electrochemical impedance spectroscopy (EIS).

2. MATERIALS and METHODS

2.1. Materials

Pinus roxburghii (Salla) wood waste was collected from indigenous carpentry shops in Kathmandu, Nepal. Analytical grade chemicals were used as received without further treatment. The activating agent for the preparation of AC was 85% phosphoric acid (H_3PO_4) with a specific gravity of 1.73 g/mL (15.0 M) obtained from Fischer Scientific, India. (P) Ltd. Double-distilled water was used throughout the experimentation. Carbon black, polyvinylidene fluoride (PVDF), and N-methyl pyrrolidone (NMP) were supplied by Sigma-Aldrich (St. Louis, MO, USA) and Fe_2O_3 was gotten from APS Ajax Finechem (Seven Hills, Australia). Additionally, Ni-foam was obtained from PRED MATERIALS, International (New York, NY, USA).

2.2. Methods

2.2.1. Synthesis of activated carbon (AC)

Firstly, the collected wood waste was sun-dried for a few days. In the preliminary stages, the sun-dried sample was air-dried, crushed, milled, ground, and screen-sieved. The particle sizes were controlled by sieving with a 150 μm size sieve to obtain a fine wood powder that was used as a precursor for the preparation of AC.

AC was synthesized using a previously reported protocol (Kim and Kim, 2020; Özcan and Korkmaz, 2019; Shrestha, 2021; Shrestha *et al*., 2019) in which the precursor was impregnated chemically with H_3PO_4 in a ratio of 1:1, i.e., the weights of the precursor and activating agent were 1:1 (w/w), and subsequently kept at room temperature for 24 h for proper soaking. Afterward, the resulting sample was dried using evaporation methods at 110℃ for 2 h in an oven. Thereafter, the carbonization process was started by inserting the sample into a tubular furnace at 400℃ for 3 h in a continuous N_2 flow at 100 mL/min. Subsequently, the carbonized samples were cooled to room temperature by maintaining the N_2 atmosphere. Afterward, the cooled samples were washed with hot distilled water severally to remove impurities fast and subsequently washed with cold distilled water till the measured pH was neutral. Finally, the samples were dried at 110℃ (Hwang *et al*., 2021b; Lee *et al*., 2021; Shrestha and Rajbhandari, 2021), ground, and used for physical and electrochemical characterizations. The samples are represented as prepared activated carbon (Pr-AC).

2.3. Physical characterization of prepared activated carbon (Pr-AC)

An SDT Q600 V20.9 Build 20 USA thermogravimetric analyzer was used for the thermogravimetric analysis/differential scanning calorimetry (TGA/DSC) analysis of the raw wood powder (Pr-R). Pr-AC was characterized using different instrumental techniques: XRD (RIGAKU X-ray diffractometer, RIGAKU, Tokyo, Japan) was used to study the phase state of Pr-AC, and defects were examined using Raman spectra (labRAM HR800 France, JOBIN YVON, Edison, NJ, USA). The oxygen content of Pr-AC was inspected using FTIR (BRUKER-

OPTIK GMBH, Ettlingen, Germany; Vertex 70/80, Bruker, Billerica, MA, USA) and an XPS (MultiLab 2000, Thermo Fischer Scientific, Waltham, MA, USA) system with an Al Kα source at 1.487 kV and 200 W. The surface area and pore volume were analyzed using the BET (Micromeritics ASAP 2020 system, Micromeritics, Norcross, GA, USA) method and SEM (Mini SEM nanoeyes, Tesko, Daegu, Korea) was used to identify the surface morphology of Pr-AC.

2.4. Fabrication of electrodes

The synthesis of Pr-AC-electrode-material was as follows: A mixture of 8 mg of Pr-AC (powder), 1 mg of carbon black powder, and 1 mg of PVDF were ground in a mortar. Thereafter, 200 μL of NMP solution was added to the mixture to dissolve PVDF. The mixture was ground thoroughly and the resulting paste was the electrode material. Afterward, approximately 70 μL of the paste was applied to a rectangular-shaped Ni-foam of 1 cm^2 area.

Similarly, hybrid composite electrodes (HCEs) were fabricated. The active materials for the hybrid composites were Pr-AC and Fe_2O_3 in 3 Pr to Fe_2O_3 mixed ratios of 1:1, 1:2, and 2:1. Finally, the fabricated electrodes namely: Pr-AC-electrode, HCEs (1:1, 2:1, and 1:2), and Fe_2O_3-electrode, were oven-dried at 70℃ overnight, pressed individually at 10 kPa pressure for 1 min, and soaked overnight in 6 M KOH solution before electrochemical measurements. Thereafter, electrical contact with the electrode was made through a Cu wire.

2.5. Electrochemical characterizations

The electrochemical performances of the fabricated electrodes were tested individually in a 6 M KOH solution using a 3-electrode experimental setup consisting of Pr-AC-electrode, HCEs, and Fe_2O_3-electrode separately as working electrodes, a Pt plate as a counter electrode, and Ag/AgCl as a reference electrode. The cell was connected to a Metrohm Autolab (PGSTAT 302 N) potentiostat/galvanostat system and the experiment was performed at room temperature.

A potential window of −1 to −0.2 V was chosen for CV measurement of Pr-AC-electrode and −1.15 to −0.4 V for HCEs, and varying scan rates of 2, 5, 10, 20, 50, and 100 mV s^{-1} were used. GCD testing was observed over the same potential window, employing current densities of 1, 2, 3, 5, 10, 15, and 20 Ag^{-1}, and the cyclic stability (% retention) was estimated from the GCD analysis. A frequency range of 100 kHz to 0.1 Hz was used at a perturbation signal of 10 mV for EIS measurements, and a Nova 1.1 software was used to fit the EIS data (Ding *et al*., 2020; Shrestha, 2021; Shrestha *et al*., 2019).

3. RESULTS and DISCUSSION

3.1. Thermal decomposition behavior of raw wood dust powder of *Pinus roxburghii*

TG/DSC analyses were employed to understand the thermal decomposition behavior of Pr-R as shown in Fig. 1.

Fig. 1 shows that Pr-R has a slight weight loss around 100℃ in the TG curve that may be due to moisture loss; this is verified by a sharp peak at 100℃ in the differential scanning calorimetry (DSC) curve. Furthermore, there is a contracted peak between 200℃ and 300℃ which is not seen in the TG plot. However, slight weight loss is detected in the DSC curve between 200℃ and 300℃ that is attributed to the complete breakdown of hemicellulose between 300℃ to 310℃ (Gao *et al*., 2017; Hwang *et al*., 2021a). Between 300℃ and 400℃ on the TG curve, a noteworthy weight loss that is confirmed at 390℃ in the DSC curve is seen. This means that cellulose starts to break down at 300℃ and is transformed into organic volatile matter present in raw wood dust powder at 400℃. The TG curve shows that the

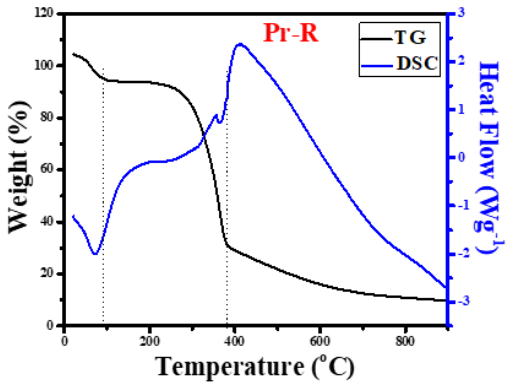

Fig. 1. TGA/DSC curves for Pr-R. TGA/DSC: thermogravimetric analysis/differential scanning calorimetry.

wood dust powder is steadier beyond 400℃ (Shrestha and Rajbhandari, 2021), whereas in the DSC curve depressions (endothermal peaks) are seen around 50℃ and 390℃. No depressions are seen in other parts of the curve; hence, a heating rate of 400℃ is postulated to be adequate for carbonization.

The amount of precursor left after carbonization at 400℃ is approximately 50%, i.e., 50% is lost in the process as shown in Fig. 1.

3.2. Characterization of prepared activated carbon (Pr-AC)

3.2.1. XRD

The XRD profiles for Pr-AC are shown in Fig. 2(a). The broad diffraction peaks centered around 23.5° and 43.5° correspond to the (002) and (100) planes of AC (Gao *et al*., 2016), respectively. The amorphous nature of carbon is identified through the broad peaks (Molina-Sabio *et al*., 1995), and there is no observed sharp peak because of the absence of degree of graphitization (Liu *et al*., 2016; Wang *et al*., 2013). However, in some cases, insignificant peaks can be seen that may be due to the presence of impurities or moisture associated with the sample.

3.2.2. Raman spectra

Raman spectra studies in Fig. 2(b) verify the amorphous nature of Pr-AC shown by the XRD profiles**.** Two relatively sharp peaks that are G and D bands at 1,589 cm^{-1} and 1,340 cm^{-1}, respectively, are seen and the relative intensity ratio of the D band to the G band is approximately 1, indicating irregularity in the lattice space or a disordered carbon structure. Gao *et al*. (2017) reported that in contrast to crystalline materials, amorphous materials have a large number of vacancy-like structural defects (no regular atomic structure) that facilitate the diffusion of electrolyte ion and electrochemical reactions (Gao *et al*., 2016). Furthermore, amorphous materials experience isotropic stress and strain of charge –discharge that helps in better cycling stability.

3.2.3. SEM

SEM micrographs of the internal structure of Pr-AC at a magnification of x2.0k showing well-developed highly porous morphology with well-developed pores are illustrated in Fig. 2(c). The development of pores on the surfaces of Pr-AC is due to dehydration by H_3PO_4 and subsequent reaction with oxygen to generate phosphoric anhydride (P_2O_5). When P_2O_5 sublimated from solid to gas at a temperature of 360℃, gaseous P_2O_5 escaped by creating pores on the carbon surface (Ju *et al*., 2020; Sarkar *et al*., 2015). The remaining P_2O_5 was hydrolyzed and removed by micropores and mesopores creating vacant spaces equal to the amount of phosphoric acid removed (Xie *et al*., 2018).

3.2.4. BET analysis

The properties of the surface area and porosity of Pr-AC were evaluated using BET analysis [Fig. 2(d)] and the summarized results are presented in Table 1. N_2 adsorption-desorption isotherms present type II behavior according to the Brunauer-Deming-Deming-Teller (*BDDT*) classification (Brunauer *et al*., 1938; Kondrat *et al*., 2012), indicating a strong presence of mesopores and a

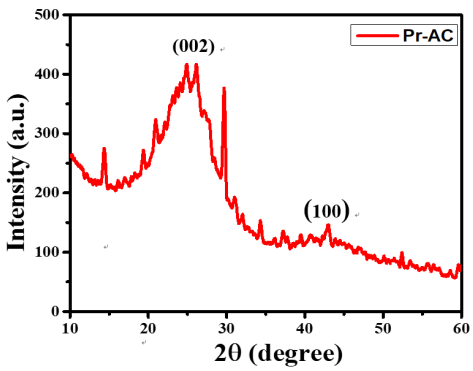

(a)

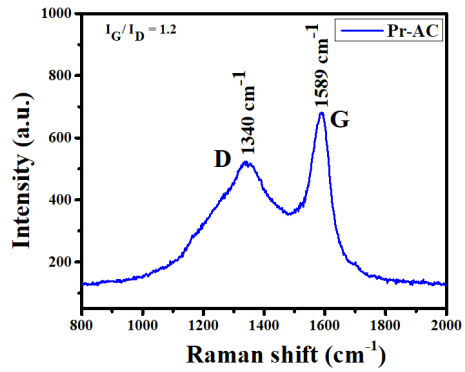

(b)

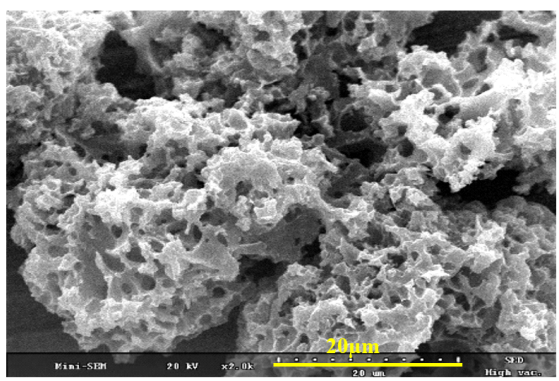

(c)

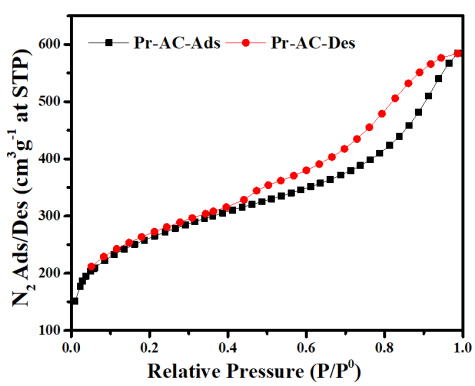

(d)

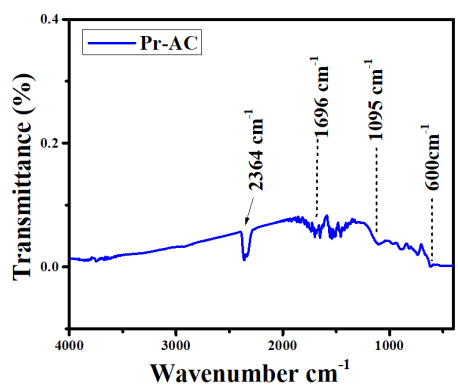

(e)

Fig. 2. Physical characterization of prepared activated carbon. (a) XRD pattern of Pr-AC, (b) Raman spectra of Pr-AC, (c) SEM image of Pr-AC, (d) N_2 adsorption/desorption isotherms of Pr-AC at 77 K, (e) FTIR spectra of Pr-AC. XRD: X-ray diffraction, Pr-AC: prepared activated carbon, SEM: scanning electron microscopy, FTIR: Fourier transform infrared spectroscopy.

Table 1. BET specific surface area, pore size, and pore volume of Pr-AC

AC	Specific surface area (m^2/g)	Pore size (BJH Ads) (nm)	Pore volume (BJH Ads) (cm^3/g)
Pr-AC	916.23	3.96	0.69

BET: Brunauer–Emmett–Teller, Pr-AC: prepared activated carbon.

proportion of micropores.

The BET investigation discloses that in Pr-AC, the isotherms show a small nitrogen uptake at low pressure ($P/P° < 0.1$), signifying the existence of limited microporosity. Conversely, the amount of nitrogen uptake starts from the relative pressure ($P/P°$) of 0.4 and is augmented, displaying a hysteresis loop throughout the process of nitrogen adsorption and desorption of up to 1.0 ($P/P°$). This indicates the presence of enormous mesoporosity in Pr-AC. Such pores are also noticeable in the SEM image [Fig. 2(c)]. The results obtained from BET measurement are shown in Table 1.

Pr-AC exhibits a surface area of 916.23 m^2/g, pore size of 3.96 nm, and pore volume of 0.69 cm^3/g. The SEM micrograph of Pr-AC [Fig. 2(c)] shows a highly porous structure, and such porosity could be interrelated. The porosity may be attributed to the release of P_2O_5 during carbonization and the washing phases that generate immense pores (Pankaj *et al*., 2018). Porous carbon materials have the advantages of large specific surface area, high conductivity, stable structure, and relatively low price, making them ideal electrode materials for supercapacitors (Duan *et al*., 2020).

3.2.5. FTIR

Fig. 2(e) displays the FTIR spectra of Pr-AC. The peak at 2,364 cm^{-1} corresponds to the –OH stretching of carboxyl, phenol, alcohol vibration, and adsorbed water. The existence of this peak indicates improved functionalization in raw wood dust after H_3PO_4 activation (Duan *et al*., 2020). The peak at 1,696 cm^{-1} is attributed to olefinic C = C vibrations in aromatic rings (Liu *et al*., 2016). The peak at 1,095 cm^{-1} is caused by the stretching of -C–O bonds in acids, alcohols, phenols, ethers, and esters (Li *et al*., 2020). The peak near 600 cm^{-1} is ascribed to C–C stretching in the fingerprint region. These show that plenteous oxygen-containing groups are formed on Pr-AC because of chemical oxidation. The FTIR results show that Pr-AC is abundantly functionalized with oxygen-containing functional groups, such as carboxylic, ether, and phenolic groups after H_3PO_4 activation.

3.2.6. XPS

The distributions of carbon and oxygen on the AC surface can be derived from the C 1s and O 1s spectra, respectively. To reveal additional evidence about the surface chemistry and binding natures of carbon and oxygen on Pr-AC, XPS spectra measurements were taken as shown in Fig. 3(a–c). Typical XPS survey spectrum of Pr [Fig. 3(a)] exhibits C 1s, O 1s, and P 2p peaks with no other detected elemental peaks, revealing that the Pr-AC comprises 3 main elements: C, O, and a trace amount of P.

Fig. 3(b) shows the C 1s signals of Pr-AC. The maximum C 1s signal on Pr-AC shifts to higher binding energy due to an increase in oxidic species (alcohols and carboxylic groups) and ethers on the carbon surface after acid treatment (Li, 2012). Fig. 3(b) shows the broad peak of C 1s. On deconvolution, 3 peaks are positioned at binding energies (BE) of 283.1 eV for C–C which is for a nonfunctionalized carbon, 284.2 eV for ether and alcohol (R-O-R/-OH), and 287.0 eV for aldehyde and ketone (-CHO/C = O; Maile *et al*., 2019). Three deconvoluted oxygen peaks (O 1s) are assigned to phosphatic oxygen (PO_4^{3-}) at 531.1 eV, a hydroxyl group (-OH) at 533.2 eV, and silicon dioxide (SiO_2) at 533.1 eV. The broad peaks observed indicate an overlap of various functional groups. Fig. 3(a) and (b) confirm that

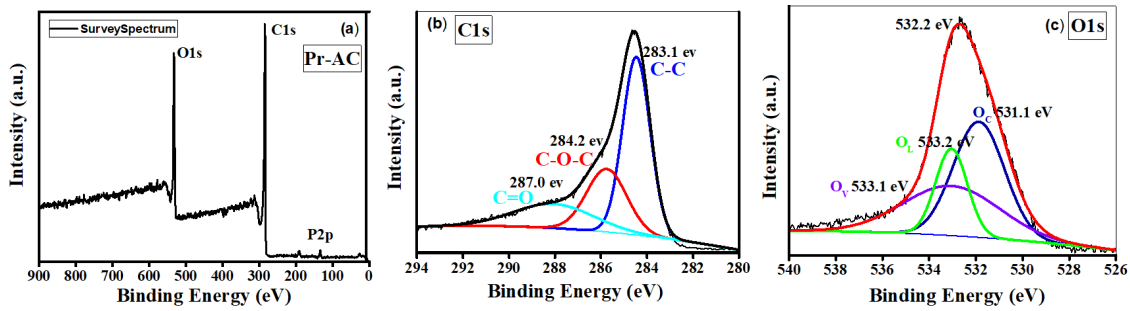

(a) (b) (c)

Fig. 3. XPS spectra. (a) XPS spectra of Pr-AC, (b) XPS spectra of C 1s on the Pr-AC surface, and (c) XPS spectra of O 1s on the Pr-AC surface. XPS: X-ray photoelectron spectroscopy, Pr-AC: prepared activated carbon.

Pr-AC is finely functionalized after H_3PO_4 activation and comprises more acidic functional groups, such as aldehydes/ketones, ethers, and hydroxides (Maile *et al*., 2019). The results reveal that the breakdown of cellulose, hemicellulose, and lignin, cross-linking of H_3PO_4, and functionalization occur as a consequence of carbonization and activation. Carbon and oxygen are present in Pr-AC, and Wong *et al*. reported that when the carbon and oxygen-containing AC is used as an electrode material for a supercapacitor, it helps to increase the pseudocapacitance and cycling stability (Wong *et al*., 2020). Summarily, Pr-AC is amorphous, highly porous with enormous mesoporosity, and has a large surface area and oxygenated functional groups that are the required characteristics of ACs used as electrode materials. This motivated the application of *Pinus roxburghii* derived AC, Pr-AC, as electrode materials for supercapacitors.

3.2.7. X-ray diffraction (XRD) of hybrid composites

The XRD pattern of the 1:1 hybrid composite of Pr-AC:Fe_2O_3 (Fig. 4) shows diffraction peaks for α-Fe_2O_3 at 24°, 34°, 36°, 42°, 50°, 54°, 57°, 63°, and 65°, corresponding to the (012), (104), (110), (113), (024), (116), (018), (214), and (300) planes, respectively. Wang *et al*. (2019) reported that the XRD pattern for pure α-Fe_2O_3 shows a main peak at 33°, corresponding to the (104) plane which is an indication of the formation of the Fe_2O_3 phase (Wang *et al*., 2009). All the peaks observed in Pr-AC:Fe_2O_3 show the formation of a homogenous composite and they are mostly lattice parameters of the composites calculated from the diffraction peaks at (104) and (110) planes that agree with JCPDS no. 89-8104 (Zhang *et al*., 2015).

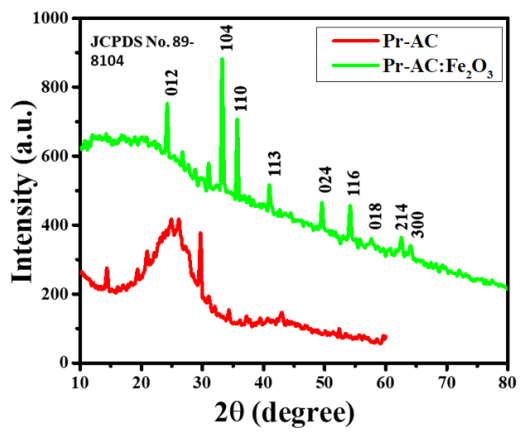

Fig. 4. XRD pattern for Pr-AC and Pr-AC:Fe_2O_3. XRD: X-ray diffraction, Pr-AC: prepared activated carbon.

3.3. Electrochemical performances of the electrodes

3.3.1. Cyclic voltammetry (CV) study

The CV curves of Pr-AC-electrode at different scan rates of 2, 5, 10, 20, 50, and 100 mV s^{-1} at potential windows of −1.2 to −0.1 V, −1.1 to 0.0 V (Figures not shown), and −1 to −0.2 V in 6 M aqueous KOH electrolyte were observed. Among them, the potential window of −1 to −0.2 V was most suitable based on the current density and shape of the CV curves [Fig. 5(b)]. The Pr-AC-electrode exhibited quasi-rectangular shapes in their CV curves without obvious distortion, indicating their reversibility. The high scan rate did not distort the features of the CV (Zequine *et al*., 2017).

The CV curve of the Pr-AC-electrode at a scan rate of 100 mV s^{-1} shows performance similar to the rectangular cyclic performance of an ideal capacitor with no redox peak that enables easy and smooth passage of electrolyte ions. Hence, no redox peaks are observed in the CV curves, and the charge storage mechanism in Pr-AC-electrode seems to be due to the EDLC mechanism (Mondal *et al*., 2017). The current density is approximately 6 Ag^{-1}. From Fig. 5, the negative potential limit can be fixed at −1.15 V as there is an increase in the current above this potential due to an H_2 evolution reaction, which needs to be avoided. However, the value acquired from CV is not so noteworthy when compared with those from other studies (Puziy *et al*., 2002). Therefore, for the enhanced electrochemical performances of Pr-AC, its hybrid composite with Fe_2O_3 was studied, and its electrochemical capacitive behaviors were investigated.

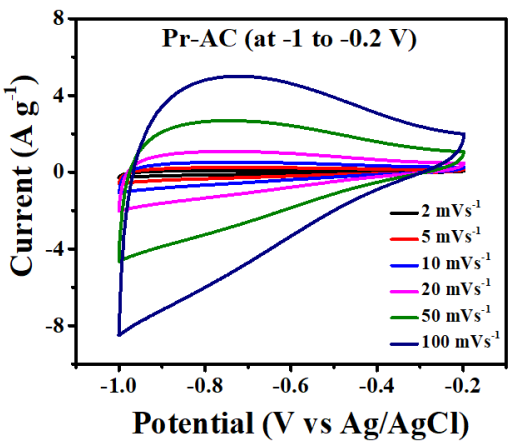

Fig. 5. CV measurements of Pr-AC-electrode at different scan rates at a potential window of −1 to −0.2 V. CV: cyclic voltammetry, Pr-AC: prepared activated carbon.

Many potential windows were tried for HCEs; however, the potential window of −1.15 to 0.4 V was found to be the best, with all 3 (1:1, 1:2, and 2:1) HCEs displaying rectangular EDLC curves and redox peaks as shown in Fig. 6. Nevertheless, when the amount of Fe_2O_3 was doubled, the capacitance declined, which may be due to the accretion of the Fe_2O_3 particles inside the composite or due to the high bulk resistance value of pure Fe_2O_3 [Fig. 6(b); Chakraborty *et al*., 2020].

When the quantity of Fe_2O_3 was halved, the redox peak almost disappears and the rectangular shape of EDLC becomes dominant, as shown in Fig. 6(c). This demonstrates that the redox feature of the composite electrodes practically depends on the quantity of Fe_2O_3 since redox reactions take place on Fe_2O_3. The redox reactions are due to the reversible conversion of Fe^{3+} to Fe^{2+} (Chakraborty *et al*., 2020; Kim and Kim, 2020); therefore, introducing Fe_2O_3 into the electrode material imparts pseudocapacity. However, in 1:1 (Pr-AC:Fe_2O_3), the redox behavior seems moderate which may be due to the saturation of Fe_2O_3 particles within the composite.

3.3.2. GCD study

The electrochemical properties of Pr-AC-electrode are studied further using a GCD process at the same potential window of −1 to −0.2 V as shown in Fig. 7.

Fig. 7 shows that at a low current density the GCD curve is nearly triangular; however, the curve still shows

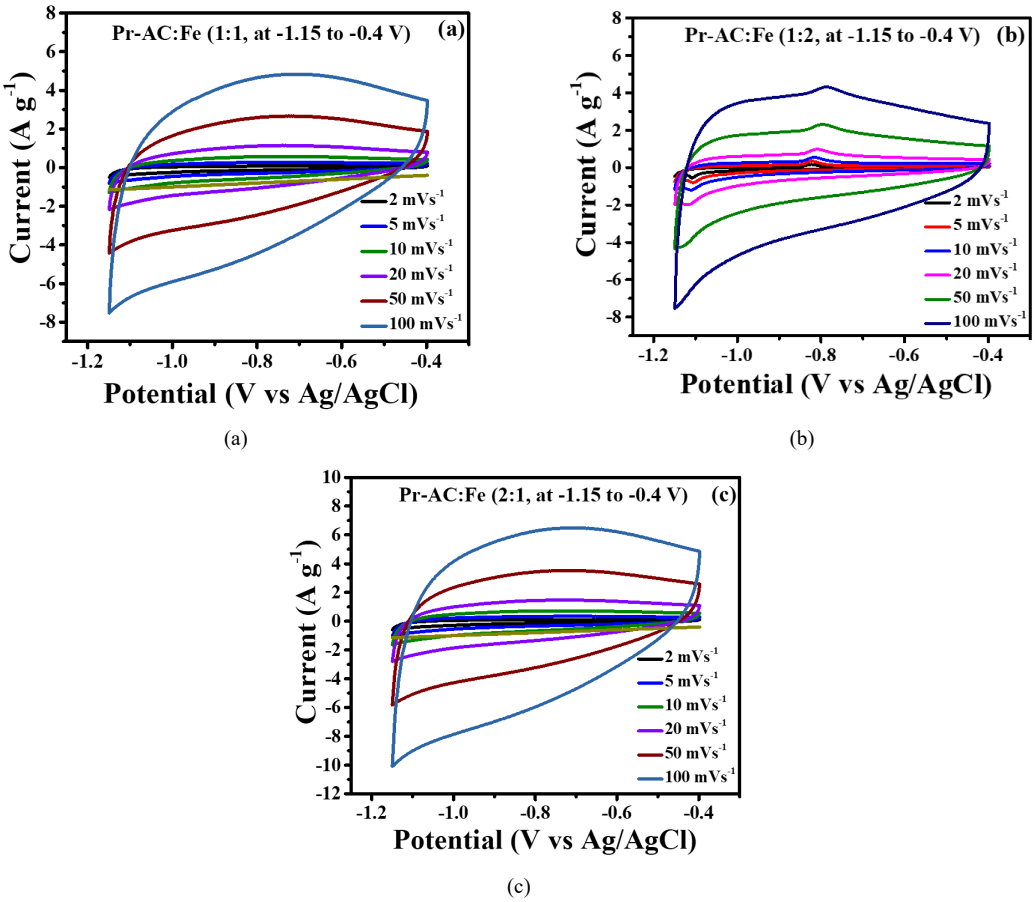

Fig. 6. CV measurements of HCEs. (a–c) CV curves of 3 different ratios of (Pr-AC:Fe_2O_3)-HCEs at a potential window of −1.15 to −0.4 V. CV: cyclic voltammetry, Pr-AC: prepared activated carbon, HCE: hybrid composite electrodes.

symmetry, indicating the high charge–discharge reversibility of the sample material.

Afterward, the HCEs (Pr-AC:Fe_2O_3) were studied further using a GCD process in the −1.15 to −0.4 V potential window. The GCD curves for HCEs are shown in Fig. 8(a–c). The GCD curves have an approximately triangular shape at low current density with a bending nature due to redox reactions in the pseudocapacitor material (Xuan *et al.*, 2020). Irrespectively, the GCD curve retains symmetry owing to reversibility in the charge–discharge behavior of the material. The discharge time for the composites decreased with increasing amounts of Fe_2O_3 (70 s for 2:1, 60 s for 1:1, and 50 s for 1:2).

The specific capacitances of all the fabricated electrodes were calculated using Equation (1) (Sarangapani *et al.*, 1996):

$$C_{SP} = \frac{I\triangle t}{m\triangle V} \quad (1)$$

where I (A) is the discharge current, $\triangle t$ (s) is the discharge time consumed in the potential window of

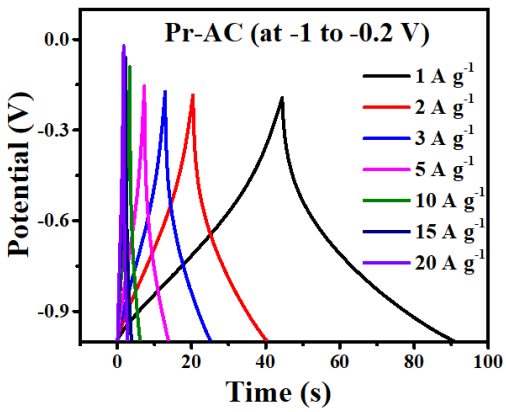

Fig. 7. GCD of Pr-AC-electrode at the potential window −1 to −0.2 V. Pr-AC: prepared activated carbon.

$\triangle V$(V), and m (g) is the mass of active material.

The specific capacitance of Pr-AC-electrode was 59.02 Fg^{-1}. However, the specific capacitances of hybrid composites were higher at 102.2 Fg^{-1} for the 2:1 ratio, as shown in Table 2. The better specific capacitance value of 2:1 HCEs compared with that of the Pr-AC-electrode may be due to the homogenous distribution of Fe_2O_3 on porous Pr-AC or low resistance, which is further discussed with the EIS analysis.

3.3.3. Effect of current density on the specific capacitance

The effect of current density on the specific capaci-

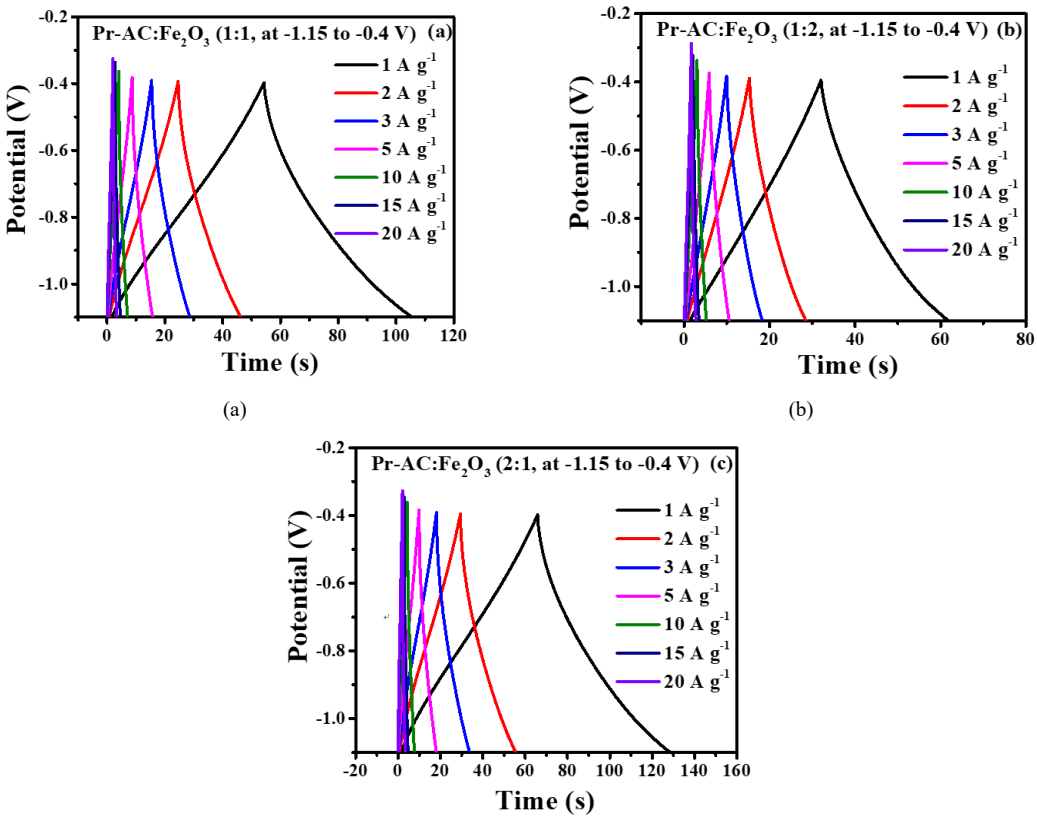

(a) (b)

(c)

Fig. 8. GCD of HCEs. (a–c) GCD curves for 3 different ratios of (Pr-AC:Fe_2O_3)-HCEs at a potential window of −1.15 to −0.4 V. Pr-AC: prepared activated carbon, HCE: hybrid composite electrodes.

Table 2. Specific capacitances from GCD at different current densities

Current density (Ag^{-1})	Specific capacitance (C_{sp}) (Fg^{-1})			
	Pr-AC-electrode	1:1	1:2	2:1
1	59.02	82.42	49.04	102.22
2	51.38	68.08	41.73	82.76
3	47.69	62.27	39.23	74.62
5	43.37	55.85	36.43	65.99
10	37.74	48.78	35.41	55.73
15	34.76	45.42	34.01	50.20
20	33.30	43.85	33.63	47.17

Pr-AC: prepared activated carbon.

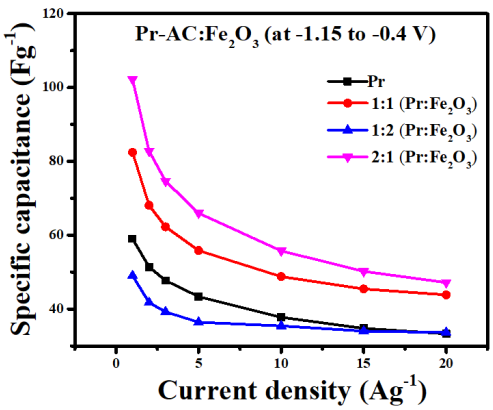

Fig. 9. The specific capacitances of Pr-AC-electrode and (Pr-AC:Fe_2O_3)-HCEs as a function of current density. Pr-AC: prepared activated carbon, HCE: hybrid composite electrodes.

tance is displayed in Fig. 9. The curve shows a sharp decline in the specific capacitance at a current density of up to 10 Ag^{-1} in all electrodes except 1:2 HCE; thereafter, the current density is approximately constant. At 1 Ag^{-1}, 1:2 HCE showed the lowest specific capacitance of 49.04 Fg^{-1}, while 2:1 HCE showed the highest of 102.22 Fg^{-1}, showing more than double enhancement of the specific capacitance. At 20 Ag^{-1}, the enhancement of the specific capacitance is only about 1.4 times because the higher current density limits the diffusion of ions into the inner pores of the electrodes, leading to a lowering of the specific capacitance (Lee and Goodenough, 1999). The specific capacitances of Pr-AC-electrode and HCEs at different current densities are shown in Table 2.

3.3.4. Capacity retention (%)

The life cycle or stability of the fabricated electrodes was investigated using capacity retention (%). In this study, 1,000 continuous charge–discharge cycles were applied at a current density of 3 Ag^{-1}. The comparison of the capacity retention (%) of Pr-AC-electrode, (Pr:Fe_2O_3)-HCEs, and Fe_2O_3-electrode are shown in Fig. 10.

Fig. 10 shows that the Pr-AC-electrode has a poor retention capacity of 67.4%. However, the benefit of compositing the Pr-AC-electrode with Fe_2O_3 in the 2:1 ratio is noticeable from its high retention capacity of 94.4%. Contrarily, the 1:1 and 1:2 Pr-AC:Fe_2O_3-HCEs show somewhat low retention capacity than the 2:1 composition. This can be explained by the presence of a higher amount of Fe_2O_3 which exhibits a low retention capacity of 73.1% at the end of 1,000 charge–discharge cycles. The lower retention capacity of Fe_2O_3 is due to its high equivalent series resistance (ESR) value. The

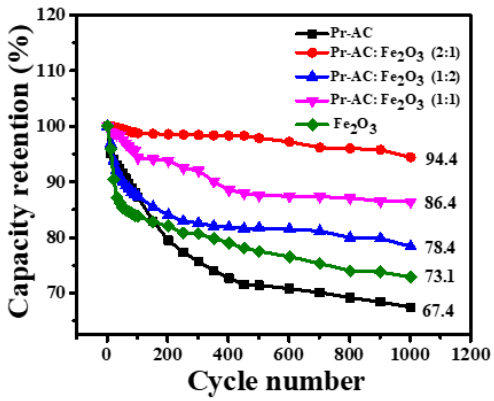

Fig. 10. Capacity retention (%) of Pr-AC-electrode, (Pr-AC:Fe_2O_3)-HCEs, and Fe_2O_3-electrode. Pr-AC: prepared activated carbon, HCE: hybrid composite electrodes.

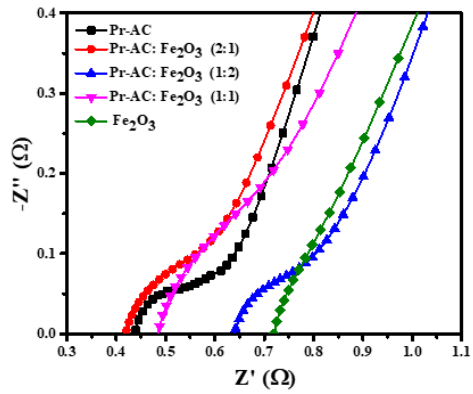

Fig. 11. Nyquist plots of Pr-AC-electrode, (Pr-AC: Fe_2O_3)-HCEs, and Fe_2O_3-electrode at a frequency range of 100 kHz to 0.1 Hz and perturbation signal of 10 mV AC voltage in 6 M KOH aqueous solution. Pr-AC: prepared activated carbon, HCE: hybrid composite electrodes.

best retention capacity of 2:1 Pr-AC:Fe_2O_3-HCEs indicates electrochemical stability of the material due to excellent electrical conductivity (least ESR among all) and low degradation of the composite (Shrestha, 2021; Shrestha and Rajbhandari, 2021; Shrestha *et al*., 2019). The cycling of potential results in the degradation of electrode materials and causes an increase in the ESR value, lowering the capacity retention (Maile *et al*., 2019).

3.3.5. Electrochemical impedance spectroscopy (EIS) analysis

EIS measurements for Pr-AC-electrode, (Pr-AC:Fe_2O_3)-HCEs, and Fe_2O_3-electrode were carried out to analyze the resistive component in the system, and the results are depicted in Fig. 11.

Fig. 11 shows that in high-frequency regions a semicircular loop is formed from which the ESR can be estimated as the total ESR due to electrode and electrolyte. A straight line at the low-frequency region is due to diffusion and transportation of electrolytes into the porous site on the electrodes.

The different ESR values in the Nyquist plots display the effect of the ratios of the composite materials. The results show that compositing Pr-AC-electrode visibly increases its ESR value; the 2:1 composite has the least ESR value of 0.42 Ω while the 1:2 composite has the highest of 0.64 Ω. The ESR value for Fe_2O_3-electrode is higher (0.73 Ω) than that for the (Pr-AC:Fe_2O_3)-HCEs as seen in Fig. 11. Therefore, the composition of the electrodes is a chief feature in developing the resisting component of the electrode.

3.3.6. Power and energy density evaluation

The Ragone plots of all fabricated electrodes evaluated from GCD measurements at a potential window range of −1.15 to −0.4 V are shown in Fig. 12. The energy and power densities of all fabricated electrodes are calculated using Equations (2) and (3) and the results are presented in Table 3.

$$E = \frac{1}{8} C_{SP} \triangle v^2 \quad (2)$$

$$P = \frac{E}{\triangle t} \quad (3)$$

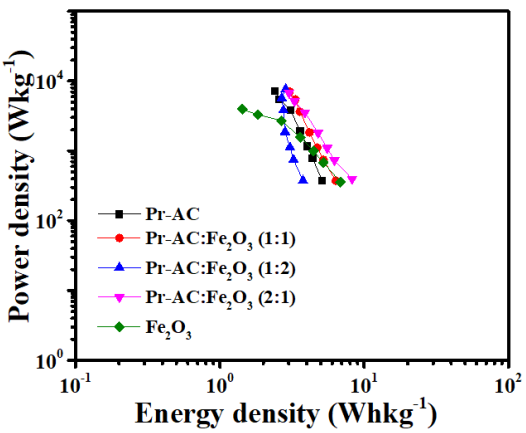

Fig. 12. Ragone plots of Pr-AC–electrode, 3 ratios of (Pr-AC:Fe_2O_3)-HCEs, and Fe_2O_3-electrode. Pr-AC: prepared activated carbon, HCE: hybrid composite electrodes.

where E is the energy density in Whkg^{-1}, P is the power density in Wkg^{-1}, C_{SP} is the specific capacitance in Fg^{-1}, $\triangle V$ is the potential window, and $\triangle t$ (s) is the discharge time. In this study, a 3-electrode system was used to measure the electrochemical performances, and the energy density was derived from dividing the C_{SP} by 8 instead of 2.

The calculated energy density for the 1:1, 1:2, and 2:1 hybrid composites (Pr-AC:Fe_2O_3) were 6.46 Whkg^{-1} at a power density of 372.75 Wkg^{-1}, 4.3 Whkg^{-1} at a power density of 373.88 Wkg^{-1}, and 8.29 Whkg^{-1} at a power density of 395.15 Wkg^{-1}, respectively, which are higher than the value for Pr-AC which is 5.12 Whkg^{-1} at a power density of 371.33 Wkg^{-1}. Fe_2O_3 having pseudocapacitive behavior resulted in the enhancement of the energy and power densities through a fast and reversible faradaic process (Maile *et al*., 2019). The layered Fe_2O_3 structure allows intercalation and deintercalation of alkali metal ions (K^+) during redox reactions between the Fe^{3+} and Fe^{2+} oxidation states. The surface adsorption mechanism of K^+ on Fe_2O_3 may also be another probable reason for the enhanced energy and power densities in composites (Wei *et al*., 2020).

The results of specific capacitances, energy densities, power densities, capacity retention (%), and ESR values of Pr-AC-electrode, (Pr-AC:Fe_2O_3)-HCEs, and Fe_2O_3-electrode are summarized in Table 3.

4. CONCLUSIONS

In this study, *Pinus roxburghii* wood-waste derived AC was successfully prepared and characterized as supercapacitor electrode material. AC presented a BET-specific surface area of 916.23 m^{2}g^{-1} and heterogeneous surface chemical composition. This heterogeneity was

Table 3. Specific capacitances, energy densities, power densities, and ESR values for Pr-AC-electrode, (Pr-AC:Fe_2O_3)-HCEs, and Fe_2O_3-electrode

Electrodes	Potential window (V)	Specific capacitance(Fg^{-1}) at 1 Ag^{-1}	Energy density (Whkg^{-1})	Power density (Whkg^{-1})	ESR (Ω)
Pr-AC	−1 to −0.2	59.02	5.12	371.33	0.44
1:1 (Pr-AC:Fe_2O_3)-HCEs	−1.15 to −0.4	82.42	6.36	372.75	0.47
1:2 (Pr-AC:Fe_2O_3)-HCEs	−1.15 to −0.4	49.04	3.76	373.88	0.64
2:1 (Pr-AC:Fe_2O_3)-HCEs	−1.15 to −0.4	102.22	4.34	395.15	0.42
Fe_2O_3	−1.15 to −0.4	95.75	6.82	358.21	0.73

ESR: equivalent series resistance, Pr-AC: prepared activated carbon, HCE: hybrid composite electrodes.

supported by XPS analysis results, suggesting the presence of oxygenated functional groups. A simple strategy was used to fabricate hybrid-nanocomposite electrode materials from AC and Fe_2O_3, and the electrochemical performances of the electrodes were evaluated. Due to the synergistic effect of AC and Fe_2O_3, the hybrid-nanocomposite electrode materials displayed optimum performance as supercapacitor electrode materials with an admirable capacity of 102.42 Fg^{-1} at a current density of 1 Ag^{-1}, cycling stability retaining 94.4% capacitance after 1,000 cycles (at a current density of 3 Ag^{-1}), and an energy density of 8.34 Wh/kg at a power density of 395.2 Wkg^{-1} in 6 M KOH electrolyte in a 3-electrode experimental setup, and a high working voltage of 1.55 V for 2:1 (Pr:Fe_2O_3)-HCEs.

CONFLICT of INTEREST

No potential conflict of interest relevant to this article was reported.

ACKNOWLEDGMENT

The author is grateful to the Central Department of Chemistry, Institute of Science and Technology (IOST), Tribhuvan University, Kirtipur, Nepal; Department of Chemistry, Patan Multiple Campus, Tribhuvan University, Patan Dhoka, Lalitpur, 44613, Nepal. Global Research Laboratory (GRL); Sun Moon University, South Korea; Advanced Functional Material Physics (AMP) laboratory, Suranaree University of Technology (SUT), Thailand for their support in conducting this research.

REFERENCES

Aadil, M., Zulfiqar, S., Warsi, M.F., Agboola, P.O., Shakir, I. 2020. Free-standing urchin-like nanoarchitectures of Co_3O_4 for advanced energy storage applications. Journal of Materials Research and Technology 9(6): 12697-12706.

Almendros, A.I., Martín-Lara, M.A., Ronda, A., Pérez, A., Blázquez, G., Calero, M. 2015. Physico-chemical characterization of pine cone shell and its use as biosorbent and fuel. Bioresource Technology 196: 406-412.

Arun, T., Prabakaran, K., Udayabhaskar, R., Mangalaraja, R.V., Akbari-Fakhrabadi, A. 2019. Carbon decorated octahedral shaped Fe_3O_4 and α-Fe_2O_3 magnetic hybrid nanomaterials for next generation supercapacitor applications. Applied Surface Science 485: 147-157.

Brunauer, S., Emmett, P.H., Teller, E. 1938. Adsorption of gases in multimolecular layers. Journal of American the Chemical Society 60: 309-319.

Chakraborty, S., Amal Raj, M., Mary, N.L. 2020. Biocompatible supercapacitor electrodes using green synthesised ZnO/polymer nanocomposites for efficient energy storage applications. Journal of Energy Storage 28: 101275.

Chen, J., Xu, J., Zhou, S., Zhao, N., Wong, C.P. 2016. Amorphous nanostructured FeOOH and Co–Ni double hydroxides for high-performance aqueous asymmetric supercapacitors. Nano Energy 21: 145-153.

Chen, S., Qiu, L., Cheng, H.M. 2020. Carbon-based fibers for advanced electrochemical energy storage devices. Chemical Reviews 120: 2811-2878.

Collins, J., Zheng, D., Ngo, T., Qu, D., Foster, M. 2014. Partial graphitization of activated carbon by surface acidification. Carbon 79: 500-517.

Ding, S., Li, X., Jiang, X., Hu, Q., Yan, Y., Zheng, Q., Lin, D. 2020. Core-shell nanostructured ZnO@CoS arrays as advanced electrode materials for high-performance supercapacitors. Electrochimica Acta 354: 136711.

Duan, H., Wang, T., Wu, X., Su, Z., Zhuang, J., Liu, S., Zhu, R., Chen, C., Pang, H. 2020. CeO_2 quantum dots doped Ni-Co hydroxide nanosheets for ultrahigh energy density asymmetric supercapacitors. Chinese

Chemical Letters 31(9): 2330-2332.

Fan, L.T., Lee, Y.H., Gharpuray, M.M. 1982. The nature of lignocellulosics and their pretreatments for enzymatic hydrolysis. Advances in Biochemical Engineering 23: 157-187.

Fengel, D., Wegener, G. 1983. Wood: Chemistry, Ultrastructure, Reactions. Walter de Gruyter, Berlin, Germany.

Galih, N.M., Yang, S.M., Yu, S.M., Kang, S.G. 2020. Study on the mechanical properties of tropical hybrid cross laminated timber using bamboo laminated board as core layer. Journal of the Korean Wood Science and Technology 48(2): 245-252.

Gao, B., Li, Y., Tian, Y., Gai, L. 2017. Acidified activated carbon with enhanced electrochemical performance for supercapacitors. International Journal of Electrochemical Science 12: 116-127.

Gao, S., Zhu, L., Liu, L., Gao, A., Liao, F., Shao, M. 2016. Improved energy storage performance based on gamma-ray irradiated activated carbon cloth. Electrochimica Acta 191: 908-915.

Guo, C.X., Yilmaz, G., Chen, S., Chen, S., Lu, X. 2015. Hierarchical nanocomposite composed of layered V_2O_5/PEDOT/MnO_2 nanosheets for high-performance asymmetric supercapacitors. Nano Energy 12: 76-87.

Hwang, J.W., Oh, S.W. 2020. Mechanical performances of boards made from carbonized rice husk and sawdust: The effect of resin and sawdust addition ratio. Journal of the Korean Wood Science and Technology 48(5): 696-709.

Hwang, J.W., Park, H.J., Oh, S.W. 2021a. Effect of resin impregnation ratio on the properties of ceramics made from *Miscanthus sinensis* var. *purpurascens* particle boards. Journal of the Korean Wood Science and Technology 49(4): 360-370.

Hwang, U.T., Bae, J., Lee, T., Hwang, S.Y., Kim, J.C., Park, J., Choi, I.G., Kwak, H.W., Hwang, S.W., Yeo, H. 2021b. Analysis of carbonization behavior of hydrochar produced by hydrothermal carbonization of lignin and development of a prediction model for carbonization degree using near-infrared spectroscopy. Journal of the Korean Wood Science and Technology 49(3): 213-225.

Iswanto, A.H., Tarigan, F.O., Susilowati, A., Darwis, A., Fatriasari, W. 2021. Wood chemical compositions of *Raru* species originating from central Tapanuli, North Sumatra, Indonesia: Effect of differences in wood species and log positions. Journal of the Korean Wood Science and Technology 49(5): 416-429.

Ju, Y.M., Jeong, H., Chea, K.S., Ahn, B.J., Lee, S.M. 2020. Evaluation of the amount of gas generated through combustion of wood charcoal and agglomerated charcoal depending on air ventilation. Journal of the Korean Wood Science and Technology 48(6): 847-860.

Kim, G.C., Kim, J.H. 2020. Changes in mechanical properties of wood due to 1 year outdoor exposure. Journal of the Korean Wood Science and Technology 48(1): 12-21.

Kim, K.H., Kim, J.Y., Kim, C.S., Choi, J.W. 2019. Pyrolysis of lignin obtained from cinnamyl alcohol dehydrogenase (CAD) downregulated *Arabidopsis thaliana*. Journal of the Korean Wood Science and Technology 47(4): 442-450.

Kondrat, S., Pérez, C.R., Presser, V., Gogotsi, Y., Kornyshev, A.A. 2012. Effect of pore size and its dispersity on the energy storage in nanoporous supercapacitors. Energy & Environmental Science 5(4): 6474-6479.

Krishnamoorthy, K., Pazhamalai, P., Mariappan, V.K., Nardekar, S.S., Sahoo, S., Kim, S.J. 2020. Probing the energy conversion process in piezoelectric-driven electrochemical self-charging supercapacitor power cell using piezoelectrochemical spectroscopy. Nature Communications 11: 2351.

Lee, H., Kim, S., Park, M.J. 2021. Specific surface area characteristic analysis of porous carbon prepared

from lignin-polyacrylonitrile copolymer by activation conditions. Journal of the Korean Wood Science and Technology 49(4): 299-314.

Lee, H.Y., Goodenough, J.B. 1999. Supercapacitor behavior with KCl electrolyte. Journal of Solid State Chemistry 144(1): 220-223.

Li, J., Chen, D., Wu, Q. 2019. α-Fe_2O_3 based carbon composite as pure negative electrode for application as supercapacitor. European Journal of Inorganic Chemistry 2019(10): 1301-1312.

Li, M., Yu, J., Wang, X., Yang, Z. 2020. 3D porous MnO_2@carbon nanosheet synthesized from rambutan peel for high-performing supercapacitor electrodes materials. Applied Surface Science 530: 147230.

Liu, J., Wang, J., Xu, C., Jiang, H., Li, C., Zhang, L., Lin, J., Xiang Shen, Z.X. 2017. Advanced energy storage devices: Basic principles, analytical methods, and rational materials design. Advanced Science 5(1): 1700322.

Liu, L., Niu, Z., Chen, J. 2016. Unconventional supercapacitors from nanocarbon-based electrode materials to device configurations. Chemical Society Reviews 45(15): 4340-4363.

Maile, N.C., Shinde, S.K., Patil, R.T., Fulari, A.V., Koli, R.R., Kim, D.Y., Lee, D.S., Fulari, V.J. 2019. Structural and morphological changes in binder-free $MnCo_2O_4$ electrodes for supercapacitor applications: Effect of deposition parameters. Journal of Materials Science: Materials in Electronics 30: 3729-3743.

Mohamed, I.M.A., Yasin, A.S., Liu, C. 2020. Synthesis, surface characterization and electrochemical performance of ZnO @ activated carbon as a supercapacitor electrode material in acidic and alkaline electrolytes. Ceramics International 46(3): 3912-3920.

Molina-Sabio, M., RodRíguez-Reinoso, F., Caturla, F., Sellés, M.J. 1995. Porosity in granular carbons activated with phosphoric acid. Carbon 33(8): 1105-1113.

Mondal, S., Rana, U., Malik, S. 2017. Reduced graphene oxide/Fe_3O_4/polyaniline nanostructures as electrode materials for an all-solid-state hybrid supercapacitor. The Journal of Physical Chemistry C 121(14): 7573-7583.

Özcan, C., Korkmaz, M. 2019. Determination of relationship between thermal and mechanical properties of wood material. Journal of the Korean Wood Science and Technology 47(4): 408-417.

Pankaj, A., Tewari, K., Singh, S., Singh, S.P. 2018. Waste candle soot derived nitrogen doped carbon dots based fluorescent sensor probe: An efficient and inexpensive route to determine Hg(II) and Fe(III) from water. Journal of Environmental Chemistry & Engineering 6(4): 5561-5569.

Sarkar, A., Singh, A.K., Sarkar, D., Khan, G.G., Mandal, K. 2015. Three-dimensional nanoarchitecture of $BiFeO_3$ anchored TiO_2 nanotube arrays for electrochemical energy storage and solar energy conversion. ACS Sustainable Chemistry & Engineering 3(9): 2254-2263.

Schulz, H.R., Acosta, A.P., Barbosa, K.T., da Silva Junior, M.A.P., Gallio, E., de Ávila Delucis, R., Gatto, D.A. 2021. Chemical, mechanical, thermal, and colorimetric features of the thermally treated Eucalyptus grandis wood planted in Brazil. Journal of the Korean Wood Science and Technology 49(3): 226-233.

Shen, H., Kong, X., Zhang, P., Song, X., Wang, H., Zhang, Y. 2021. *In-situ* hydrothermal synthesis of δ-MnO_2/soybean pod carbon and its high performance application on supercapacitor. Journal of Alloys and Compounds 853: 157357.

Shrestha, D. 2021. Efficiency of wood-dust of *Dalbergia sisoo* as low-cost adsorbent for rhodamine-B dye removal. Nanomaterials 11: 2217.

Shrestha, D., Maensiri, S., Wongpratat, U., Lee, S.W., Rajbhandari Nyachhyon, A. 2019. *Shorea robusta* derived activated carbon decorated with manganese dioxide hybrid composite for improved capacitive

behaviors. Journal of Environmental Chemistry & Engineering 7(5): 103227.

Shrestha, D., Rajbhandari, A. 2021. The effects of different activating agents on the physical and electrochemical properties of activated carbon electrodes fabricated from wood-dust of *Shorea robusta*. Heliyon 7(9): E07917.

Sun, N., Zhou, D., Liu, W., Shi, S., Tian, Z., Liu, F., Li, S., Wang, J., Ali, F. 2020. Tailoring surface chemistry and morphology of titanium nitride electrode for on-chip supercapacitors. ACS Sustainable Chemistry & Engineering 8(21): 7869-7878.

Wang, C., Li, H., Zhao, J., Zhu, Y., Yuan, W.Z., Zhang, Y. 2013. Graphene nanoribbons as a novel support material for high performance fuel cell electrocatalysts. International Journal of Hydrogen Energy 38(30): 13230-13237.

Wang, K., Yan, R., Tian, X., Wang, Y., Lei, S., Li, X., Yang, T., Wang, X., Song, Y., Liu, Y., Liu, Z., Guo, Q. 2019. Multi-scale biomass-based carbon microtubes decorated with Ni-Co sulphides nanoparticles for supercapacitors with high rate performance. Electrochimica Acta 302: 78-91.

Wei, J., Geng, S., Pitkänen, O., Järvinen, T., Kordas, K., Oksman, K. 2020. Green carbon nanofiber networks for advanced energy storage. ACS Applied Energy Materials 3(4): 3530-3540.

Wong, S.I., Lin, H., Sunarso, J., Wong, B.T., Jia, B. 2020. Optimization of ionic-liquid based electrolyte concentration for high-energy density grapheme supercapacitors. Applied Materials Today 18: 100522.

Xie, K., Zhang, M., Yang, Y., Zhao, L., Qi, W. 2018. Synthesis and supercapacitor performance of polyaniline/nitrogen-doped ordered mesoporous carbon composites. Nanoscale Research Letters 13: 163.

Xuan, H., Li, H., Yang, J., Liang, X., Xie, Z., Han, P., Wu, Y. 2020. Rational design of hierarchical core-shell structured $CoMoO_4$@CoS composites on reduced graphene oxide for supercapacitors with enhanced electrochemical performance. International Journal of Hydrogen Energy 45(11): 6024-6035.

Yang, C., Shi, M., Nuli, Y., Song, X., Zhao, L., Liu, J., Zhang, P., Gao, L. 2020. Interfacial electrochemical investigation of 3D space-confined $MnFe_2O_4$ for high-performance ionic liquid-based supercapacitors. Electrochimica Acta 331: 135386.

Yun, T.G., Park, M., Kim, D.H., Kim, D., Cheong, J.Y., Bae, J.G., Han, S.M., Kim, I.D. 2019. All-transparent stretchable electrochromic supercapacitor wearable patch device. ACS Nano 13(3): 3141-3150.

Zequine, C., Ranaweera, C.K., Wang, Z., Dvornic, P.R., Kahol, P.K., Singh, S., Tripathi, P., Srivastava, O.N., Singh, S., Gupta, B.K., Gupta, G., Gupta, R.K. 2017. High-performance flexible supercapacitors obtained via recycled jute: Bio-waste to energy storage approach. Scientific Reports 7: 1174.

Zhang, M., Li, X., Wang, X., Li, D., Zhao, N. 2020. Three-dimensional core-branch α-Fe_2O_3@NiO/carbon cloth heterostructured electrodes for flexible supercapacitors. Frontiers in Chemistry 7: 887.

Zhang, P., Zhang, Z., Chen, J., Dai, S. 2015. Ultrahigh surface area carbon from carbonated beverages: Combining self-templating process and *in situ* activation. Carbon 93: 39-47.

Zhang, X., Fu, Q., Huang, H., Wei, L., Guo, X. 2019. Silver-quantum-dot-modified MoO_3 and MnO_2 paper-like freestanding films for flexible solid-state asymmetric supercapacitors. Small 15(13): e1805235.